

## Solid-State NMR Investigation of the Selective Perturbation of Lipid Bilayers by the Cyclic Antimicrobial Peptide RTD-1<sup>†</sup>

Jarrold J. Buffy,<sup>‡</sup> Melissa J. McCormick,<sup>‡</sup> Sungsool Wi,<sup>‡</sup> Alan Waring,<sup>§</sup> Robert I. Lehrer,<sup>§</sup> and Mei Hong<sup>\*:‡</sup>

Department of Chemistry, Iowa State University, Ames, Iowa 50011, and Department of Medicine, University of California at Los Angeles, School of Medicine, Los Angeles, California 90095

Received December 14, 2003; Revised Manuscript Received May 28, 2004

**ABSTRACT:** RTD-1 is a cyclic  $\beta$ -hairpin antimicrobial peptide isolated from rhesus macaque leukocytes. Using <sup>31</sup>P, <sup>2</sup>H, <sup>13</sup>C, and <sup>15</sup>N solid-state NMR, we investigated the interaction of RTD-1 with lipid bilayers of different compositions. <sup>31</sup>P and <sup>2</sup>H NMR of uniaxially oriented membranes provided valuable information about how RTD-1 affects the static and dynamic disorder of the bilayer. Toward phosphatidylcholine (PC) bilayers, RTD-1 causes moderate orientational disorder independent of the bilayer thickness, suggesting that RTD-1 binds to the surface of PC bilayers without perturbing its hydrophobic core. Addition of cholesterol to the POPC membrane does not affect the orientational disorder. In contrast, binding of RTD-1 to anionic bilayers containing PC and phosphatidylglycerol lipids induces much greater orientational disorder without affecting the dynamic disorder of the membrane. These correlate with the selectivity of RTD-1 for anionic bacterial membranes as opposed to cholesterol-rich zwitterionic mammalian membranes. Line shape simulations indicate that RTD-1 induces the formation of micrometer-diameter lipid cylinders in anionic membranes. The curvature stress induced by RTD-1 may underlie the antimicrobial activity of RTD-1. <sup>13</sup>C and <sup>15</sup>N anisotropic chemical shifts of RTD-1 in oriented PC bilayers indicate that the peptide adopts a distribution of orientations relative to the magnetic field. This is most likely due to a small fraction of lipid cylinders that change the RTD-1 orientation with respect to the magnetic field. Membrane-bound RTD-1 exhibits narrow line widths in magic-angle spinning spectra, but the sideband intensities indicate rigid-limit anisotropies. These suggest that RTD-1 has a well-defined secondary structure and is likely aggregated in the membrane. These structural and dynamical features of RTD-1 differ significantly from those of PG-1, a related  $\beta$ -hairpin antimicrobial peptide.

A number of disulfide-bridged, cationic  $\beta$ -hairpin antimicrobial peptides such as protegrins (1), tachyplepsins (2), and defensins (3) are produced by mammals as part of their innate immune response to microbial attack (4, 5). These peptides exhibit well-defined three-dimensional structures in solution. Their antimicrobial activity results from their disruption of the lipid membranes of the target cells (6, 7). Although the primary and secondary structures of these  $\beta$ -sheet peptides are similar, several structural studies suggested that the specific mechanisms of their antimicrobial actions may be diverse (8–12) and are not fully understood.

Several models have been proposed for the interaction of antimicrobial peptides with lipid bilayers (13). The carpet model postulates that the peptides aggregate on the bilayer surface due to electrostatic attraction between the cationic peptide and the anionic phosphates of lipids. Above a critical concentration, the peptides fragment the bilayer, resulting

in a permeable membrane (14). Solid-state NMR<sup>1</sup> experiments on several peptides such as magainins and cecropins support the carpet model (15–17). The barrel-stave model proposes that helical membrane-spanning peptides aggregate in the bilayer to form an aqueous pore, thereby destroying the bilayer (18, 19). The toroidal pore model postulates that the peptides aggregate and form a complex with lipids such that the monolayer bends continuously through a torus-shaped pore, with the lipids tilted away from the average bilayer normal direction (7, 20). Evidence of toroidal pore formation has been reported for magainin, protegrin-1 (PG-1), and MSI-78 (8, 20–22).

RTD-1 is an 18-residue cyclic antimicrobial peptide extracted from rhesus macaque leukocytes (23). It exhibits broad-spectrum antimicrobial activity and is effective against Gram-positive and Gram-negative bacteria and fungi (23, 24). Despite the three stabilizing disulfide bonds and the cyclic character, in solution RTD-1 exhibits more flexibility in the central strand region than at the turns (25). An open-chain analogue of RTD-1 was shown to have a 3-fold lower antimicrobial activity (23, 25). This led to the hypothesis

<sup>†</sup> This work is supported by National Institutes of Health Grant GM-066976 to M.H. and Grants AI-22839 and AI-37945 to A.W. and R.I.L. M.H. thanks the Sloan Foundation for an Alfred P. Sloan Research Fellowship and the Beckman Foundation for a Young Investigator Award.

\* To whom correspondence should be addressed: Department of Chemistry, Iowa State University, Ames, IA 50011. Telephone: (515) 294-3521. Fax: (515) 294-0105. E-mail: mhong@iastate.edu.

<sup>‡</sup> Iowa State University.

<sup>§</sup> University of California at Los Angeles, School of Medicine.

<sup>1</sup> Abbreviations: RTD, rhesus  $\theta$ -defensin; NMR, nuclear magnetic resonance; CSA, chemical shift anisotropy; POPC, 1-palmitoyl-2-oleoyl-*sn*-glycero-3-phosphatidylcholine; POPG, 1-palmitoyl-2-oleoyl-*sn*-glycero-3-phosphatidylglycerol; DLPC, 1,2-dilauryl-*sn*-glycero-3-phosphatidylcholine; DMPC, 1,2-dimyristoyl-*sn*-glycero-3-phosphatidylcholine.

that the lack of a terminal charge has a strong influence on the antimicrobial activity. RTD-1 has been shown to be nearly nonhemolytic (26), contrary to the structurally similar PG-1, which exhibits mild hemolytic activity (27).

Solid-state NMR spectroscopy is an important tool for elucidating the structure and dynamics of membrane-active peptides and proteins in the lipid bilayer (28, 29). It provides a sensitive and nondestructive probe of the effects of the peptides on the lipid matrix.  $^{31}\text{P}$  NMR probes the hydrophilic headgroup region of the bilayer, while  $^2\text{H}$  NMR examines the hydrophobic center of the bilayer. We have used this approach to study the lipid-peptide interaction of PG-1 (8), which shares significant structural similarities with RTD-1. These similarities include the antiparallel  $\beta$ -hairpin structure, the presence of disulfide bonds, and a significant number of Arg residues. Despite these similarities, oriented circular dichroism and X-ray lamellar diffraction experiments suggested that RTD-1 interacts with the lipid bilayers in a manner different from that of PG-1 (12). RTD-1 thins the bilayers as it binds to the membrane surface, while PG-1 thins the bilayer when inserted into the membrane (30).

In this study, we use  $^{31}\text{P}$  and  $^2\text{H}$  NMR to investigate how lipid-RTD-1 interaction depends on the membrane composition and to gain insight into the selectivity of RTD-1 for microbial membranes as opposed to eukaryotic membranes. We compare bilayers consisting of pure zwitterionic phosphatidylcholine (PC) lipids, a mixture of PC and anionic phosphatidylglycerol (PG) lipids, and a mixture of PC and cholesterol (Chol). The PC/PG bilayer mimics the bacterial membrane, while the PC/Chol bilayer mimics the mammalian membrane. We examine how the orientational and dynamical order of the various membranes is affected by RTD-1. Information about RTD-1 structure in the bilayer is gleaned from the  $^{13}\text{C}$  and  $^{15}\text{N}$  spectra of the selectively labeled peptide.  $^{13}\text{C}$  and  $^{15}\text{N}$  chemical shifts in magic-angle spinning spectra indicate that RTD-1 is immobilized in the membrane and that its secondary structure is well-defined. Surprisingly, the peptide adopts a distribution of orientations relative to the magnetic field based on the static spectra of oriented membranes. Therefore, RTD-1 differs from PG-1 in many important respects, suggesting that even small sequence differences may cause significant changes in the mechanism of action of antimicrobial peptides.

## EXPERIMENTAL PROCEDURES

**Materials.** All lipids were purchased from Avanti Polar Lipids (Alabaster, AL) and stored as powder at  $-30^\circ\text{C}$ . These include cholesterol, 1,2-dilauryl-*sn*-glycero-3-phosphatidylcholine (DLPC), 1,2-dimyristoyl-*sn*-glycero-3-phosphatidylcholine (DMPC), 1-palmitoyl-2-oleoyl-*sn*-glycero-3-phosphatidylcholine (POPC), 1-palmitoyl-*d*<sub>31</sub>-2-oleoyl-*sn*-glycero-3-phosphatidylcholine (POPC-*d*<sub>31</sub>), and 1-palmitoyl-2-oleoyl-*sn*-glycero-3-phosphatidylglycerol (POPG). Except for DMPC, which has a gel to liquid-crystalline phase transition temperature ( $T_m$ ) of  $23^\circ\text{C}$ , the other lipids have  $T_m$  values of  $-1$  or  $-2^\circ\text{C}$ . Trifluoroethanol (TFE), chloroform, and cyclohexane were obtained from Aldrich Chemicals (Milwaukee, WI).  $^{15}\text{N}$ -labeled L-cysteine and  $^{13}\text{C}$ -labeled L-leucine were purchased from Cambridge Isotope Laboratories (Andover, MA) and converted to Fmoc derivatives by AnaSpec, Inc. (San Jose, CA). RTD-1 (GFCR-

CLCRRGVCRICTR) was synthesized, purified, oxidized, and cyclized as described previously (12). Glass cover sides ( $\sim 80\ \mu\text{m}$  thick) were obtained from Marienfeld Laboratory Glassware and cut into  $6\ \text{mm} \times 12\ \text{mm}$  rectangles.

**Preparation of NMR Samples.** Mechanically aligned membranes were prepared using a procedure similar to that of Hallock *et al.* (31). The peptide was dissolved in TFE and mixed with chloroform solutions containing appropriate amounts of lipids. The solution was dried under a stream of  $\text{N}_2$  gas, and the dry lipid film was redissolved in a chloroform/TFE (2:1) solution containing a 5-fold excess of naphthalene with respect to lipid. This was deposited onto glass slides ( $6\ \text{mm} \times 12\ \text{mm}$ ) at surface concentrations of  $0.010$ – $0.025\ \text{mg}/\text{mm}^2$ . The glass plates were air-dried for  $\sim 2\ \text{h}$ , and then vacuum-dried overnight to remove residual solvents and naphthalene. Naphthalene improves the membrane alignment, presumably by leaving a porous lipid-peptide film that allows for more rapid and complete hydration (31). The dried sample was directly hydrated with  $1\ \mu\text{L}$  of water per plate and then indirectly hydrated for 2 days at 95% relative humidity using a saturated solution of  $\text{Na}_2\text{HPO}_4$ . The DMPC samples were incubated at  $40^\circ\text{C}$ , while all others were incubated at room temperature. Immediately before the NMR experiments, the glass plates were stacked, wrapped in Parafilm, and sealed in polyethylene bags to prevent dehydration during data acquisition. Additional water was sometimes added to the plates before wrapping to ensure complete hydration. Full hydration of the lipids used in this study was previously confirmed by FT-IR measurements (32). It is also directly confirmed by the  $^2\text{H}$  quadrupolar couplings measured here. Each membrane sample typically included 20–30 glass plates. Approximately 5 mg of  $^{13}\text{C}$ - and  $^{15}\text{N}$ -labeled RTD-1 was used for the chemical shift measurements, and approximately 1 mg of unlabeled RTD-1 was used for the peptide-lipid interaction experiments.

Unoriented membrane samples for magic-angle spinning (MAS) experiments were prepared by codissolving the peptide and lipid in a TFE and chloroform solution, drying it under  $\text{N}_2$  gas, redissolving the resulting film in cyclohexane, and lyophilizing it. The dry powders were packed into 4 mm rotors and hydrated to 30–35% water by mass. The samples were restricted to the center of the rotor to reduce the radio frequency (rf) field inhomogeneity.

**Solid-State NMR Spectroscopy.** NMR experiments were carried out on a Bruker (Karlsruhe, Germany) Avance DSX-400 spectrometer operating at a resonance frequency of 162.12 MHz for  $^{31}\text{P}$ , 100.72 MHz for  $^{13}\text{C}$ , 40.58 MHz for  $^{15}\text{N}$ , or 61.48 MHz for  $^2\text{H}$ . A static double-resonance probe equipped with custom-designed rectangular coils was used for oriented-membrane experiments, while MAS experiments were conducted using a 4 mm double-resonance probe.  $^2\text{H}$  spectra were acquired using a quadrupolar echo sequence with a recycle delay of 0.5 s.  $^{31}\text{P}$  spectra were recorded using a single-pulse experiment under  $^1\text{H}$  decoupling of  $\sim 50\ \text{kHz}$  with a recycle delay of  $\sim 1.5\ \text{s}$ . Two-dimensional (2D)  $^{31}\text{P}$  exchange experiments used the conventional three-pulse sequence (33).  $^{13}\text{C}$  and  $^{15}\text{N}$  MAS spectra were collected with cross-polarization contact times of 0.5 and 1 ms, respectively. Typical line broadenings were 50–100 Hz for MAS spectra and 150–200 Hz for the static  $^{13}\text{C}$ ,  $^{15}\text{N}$ , and  $^{31}\text{P}$  spectra. The  $^{13}\text{C}$ ,  $^{31}\text{P}$ , and  $^{15}\text{N}$  chemical shifts were referenced externally

to the  $\beta$ -glycine carbonyl signal (176.4 ppm), the  $^{31}\text{P}$  signal of 85%  $\text{H}_3\text{PO}_4$  (0 ppm), and the  $^{15}\text{N}$  signal of *N*-acetylvaline (122 ppm), respectively.

**$^{31}\text{P}$  and  $^2\text{H}$  Line Shape Simulations.** To simulate the  $^{31}\text{P}$  chemical shift anisotropy (CSA) and  $^2\text{H}$  quadrupolar coupling (QC) spectra of glass-plate samples with variable bilayer normal directions due to peptide binding, we need to consider the angular dependence of the nuclear spin frequencies using appropriate coordinate transformations. Since lipids undergo fast uniaxial rotations around the local bilayer normal, the CSA and QC interactions are motionally averaged to be axially symmetric, with their unique principal axes being parallel to the local bilayer normal. In other words, only the motionally averaged principal axis system (PAS) is relevant in studies involving liquid-crystalline bilayers. Depending on the geometry of the lipid phase induced by the peptide, the bilayer normal assumes a distribution away from the macroscopic alignment axis, which is the glass-plate normal. For perfectly aligned bilayers, all bilayer normals are parallel to the alignment axis. For an isotropic powder, the bilayer normals adopt a spherical distribution. Further, the alignment axis may differ from the magnetic field: it is either  $0^\circ$  or  $90^\circ$  from the magnetic field in this study. Thus, the coordinate transformations relevant to the frequency calculation are (34)

$$\text{averaged PAS} \xrightarrow{\{\alpha, \beta, \gamma\}} \text{alignment frame} \xrightarrow{\{0^\circ, \chi, 0^\circ\}} \text{lab frame } (B_0) \quad (1)$$

The spatial part of the NMR tensors  $R_{2,0}$ , defined in the laboratory frame, is related to  $\rho_{2,0}^\lambda$ , defined in the motionally averaged PAS according to

$$R_{2,0}^\lambda = \sum_{k=-2}^2 d_{k,0}^2(\chi) d_{0,k}^2(\beta) e^{ik\gamma} \rho_{2,0}^\lambda \quad (\lambda \text{ is CSA or QC}) \quad (2)$$

where

$$\rho_{2,0}^{\text{CSA}} = \sqrt{3/2} \gamma B_0 \delta_{\text{CSA}} \quad \text{and} \quad \rho_{2,0}^{\text{QC}} = \sqrt{3/8} e^2 q Q / \hbar \quad (3)$$

where  $\delta_{\text{CSA}}$  and  $e^2 q Q / \hbar$  are the motionally averaged CSA parameter and QC parameters, respectively, and  $d_{m,n}^2$  denotes reduced Wigner rotation matrices (34). Since the motionally averaged interactions are axially symmetric, the orientational averaging does not depend on the  $\alpha$  angle in eq 1. When the alignment axis is parallel to  $B_0$ , both  $\chi$  and  $\gamma$  angles in eq 1 are  $0^\circ$ . When the alignment axis is perpendicular to  $B_0$ ,  $\chi$  is  $90^\circ$ ; then an additional Euler rotation on  $\gamma$  needs to be carried out.

The orientation distribution of the bilayer normal in the alignment frame, described by the Euler angles  $\alpha$ ,  $\beta$ , and  $\gamma$ , determines the spectral line shape. Depending on the geometry of the lipid phase, different shape factors result (35). For cylindrical or 2D planar distributions, the shape factor is  $d\beta$ , which differs from  $\sin \beta d\beta$  for an isotropic distribution.

For bilayers whose normal is mostly along the alignment axis, a Gaussian distribution function  $e^{-0.5(\beta/\sigma_\beta)^2}$  with a mosaic spread of  $\sigma_\beta$  is used in the line shape calculation (36). The mosaic width for the POPC/POPG spectrum with 4% RTD-1 was optimized to be  $13^\circ$  to simulate the  $0^\circ$  peak (see Figure 3c). To simulate  $^2\text{H}$  spectra of chain-perdeuterated POPC-

$d_{31}$ , 15 motionally averaged quadrupolar couplings corresponding to the  $\text{CD}_2$  and  $\text{CD}_3$  groups of the palmitoyl chain were co-added.  $^2\text{H}$  spectral simulations used the same mosaic spread and orientations as the  $^{31}\text{P}$  spectral simulation.

**RTD-1 Orientation Calculations.** The orientation of RTD-1 in the lipid bilayer was calculated from the  $^{13}\text{C}$  and  $^{15}\text{N}$  anisotropic chemical shifts measured in uniaxially aligned bilayers. The approach was similar to that described for PG-1 (8). We take the known  $^{13}\text{C}$  and  $^{15}\text{N}$  chemical shift principal values and principal axis orientations relative to the peptide plane and express them in the molecular frame defined by the Protein Data Bank structure of RTD-1 [heretofore called PDB frame; PDB entry 1HVZ (25)]. The magnetic field ( $B_0$ ) is described by the polar angle  $\beta$  and azimuthal angle  $\alpha$  in the same PDB-defined molecular frame. The chemical shift frequency  $\omega_{\text{CS}}$  is calculated as

$$\omega_{\text{CS}} = \sigma_{11} \cos^2 \gamma_1 + \sigma_{22} \cos^2 \gamma_2 + \sigma_{33} \cos^2 \gamma_3 \quad (4)$$

where the directional cosines are the scalar product between  $B_0$  and the chemical shift principal axes ( $\cos \gamma_i = \sigma_{ii}$ ). This yields  $^{13}\text{C}$  and  $^{15}\text{N}$  anisotropic shifts as a function of the  $B_0$  orientation ( $\alpha$  and  $\beta$ ) in the PDB frame. As long as the bilayer normal is parallel to  $B_0$ , this is also the bilayer normal direction relative to the peptide. The superposition of the orientational restraints from the  $^{13}\text{C}$  and  $^{15}\text{N}$  chemical shifts yields the allowed orientation of the peptide relative to the bilayer normal.

The input  $^{13}\text{C}$  and  $^{15}\text{N}$  chemical shift principal values were directly taken from the measured parameters from the MAS sideband spectra (Figure 9). For the carbonyl carbon,  $\sigma_{11} = 247$  ppm,  $\sigma_{22} = 182$  ppm, and  $\sigma_{33} = 92$  ppm. The  $\sigma_{33}$  axis is perpendicular to the peptide plane, which includes both the C–N and the C=O bond; the  $\sigma_{22}$  axis is  $10^\circ$  from the C=O bond in the peptide plane, and the  $\sigma_{11}$  axis is perpendicular to the  $\sigma_{22}$  and  $\sigma_{33}$  axes (37, 38). The input  $^{15}\text{N}$  principal values are as follows:  $\sigma_{11} = 222$  ppm,  $\sigma_{22} = 79$  ppm, and  $\sigma_{33} = 68$  ppm. The  $\sigma_{11}$  axis is  $17^\circ$  from the N–H bond in the peptide plane; the  $\sigma_{33}$  axis is tilted  $25^\circ$  from the peptide plane, while the  $\sigma_{22}$  axis is normal to the  $\sigma_{11}$  and  $\sigma_{33}$  axes (39–41). The PDB entry of RTD-1 contains 20 minimum-energy structures. We chose three with the smallest amount of backbone distortion for the calculations, to gain insight into the orientation uncertainties due to peptide structural variation.

The obtained  $B_0$  orientation relative to the peptide is visualized by adding a point in the PDB file with the coordinates  $(x, y, z) = (\sin \beta \cos \alpha, \sin \beta \sin \alpha, \cos \beta)$ . The line connecting the origin with this point is the  $B_0$  direction relative to the peptide. The molecule is rotated so that this  $B_0$  axis is vertical and in the plane of the screen. All molecular visualization is carried out using the Insight II Biopolymer module (Accelrys).

## RESULTS

**Interaction of RTD-1 with Phosphocholine Membranes.** Since phosphatidylcholine is common in most biological membranes, PC bilayers provide a reference for mixed membranes whose compositions mimic various organisms. We first examine the concentration dependent interaction of RTD-1 with POPC bilayers. Figure 1 shows the  $^{31}\text{P}$  spectra of one such series, where the POPC lipids were aligned in

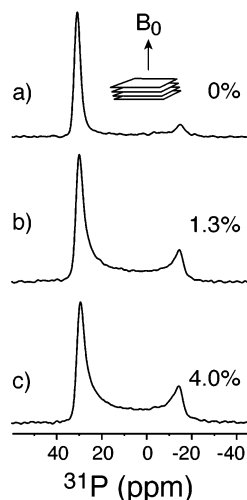


FIGURE 1:  $^{31}\text{P}$  spectra of oriented POPC bilayers with (a) 0%, (b) 1.3%, and (c) 4.0% RTD-1. The alignment axis was parallel to  $B_0$ .

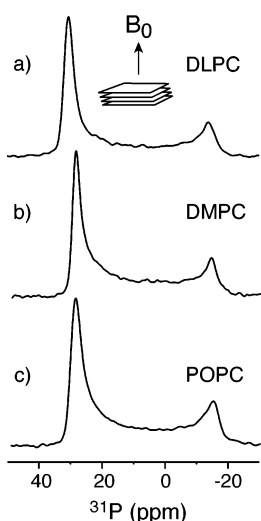


FIGURE 2:  $^{31}\text{P}$  spectra of oriented PC bilayers with 4% RTD-1 as a function of lipid chain length: (a) DLPC, (b) DMPC, and (c) POPC. The alignment axis was parallel to  $B_0$ .

the presence of an increasing amount of RTD-1. Unless otherwise specified, the alignment axis was parallel to the static magnetic field. In the absence of RTD-1, the  $^{31}\text{P}$  spectrum shows a predominant peak at 32 ppm. The addition of RTD-1 worsens the lipid orientation moderately, manifested by the increased intensity at the  $90^\circ$  edge of  $-15$  ppm. To estimate the fraction of the unoriented lipids, we compare the integrated intensities of the  $0^\circ$  peak with the rest of the spectra. To be consistent with membranes of different compositions, we assign 25% of the total chemical shift span around the  $0^\circ$  peak to the ordered phase, and the remaining chemical shift range to the disordered phase. With this criterion, we found the orientational disorder increases from 29% to 55% from the pure lipid sample to the membrane with 4% RTD-1. Within experimental uncertainty ( $\pm 5\%$ ), the 4% peptide concentration exhibits disorder similar to that of the 1.3% sample.

Next, we examine whether the lipid acyl chain lengths affect the interaction of RTD-1 with the membrane. Figure 2a–c shows  $^{31}\text{P}$  spectra of DLPC, DMPC, and POPC bilayers with 4% RTD-1. Binding of RTD-1 induced similar and moderate orientational disorder of the bilayers, shown

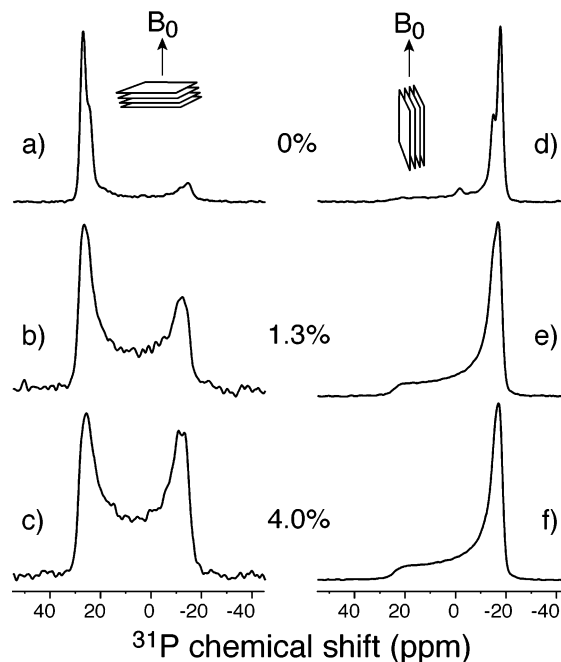


FIGURE 3:  $^{31}\text{P}$  spectra of oriented POPC/POPG (3:1 molar ratio) bilayers in the presence of no RTD-1 (a and d), 1.3% RTD-1 (b and e), and 4.0% RTD-1 (c and f). The alignment axis was alternately parallel (a–c) and perpendicular (d–f) to  $B_0$ .

by the similar intensity of the unoriented lipids relative to that of the whole spectrum. In other words, there is no clear correlation between the amount of orientational disorder and the bilayer thickness. This contrasts with PG-1 (8), which is drastically more disruptive to POPC bilayers than to DLPC bilayers. The chain length independence of RTD-1–lipid interaction suggests that RTD-1 binds to the membrane surface with minimal insertion into the bilayer (*vide infra*).

*Interaction of RTD-1 with Anionic Phospholipid Membranes.* To understand the interaction of RTD-1 with bacterial membranes, we prepared a mixture of POPC and POPG lipids with a molar ratio of 3:1. Typically, 2–5 mg of the total POPC was chain-perdeuterated (POPC- $d_{31}$ ) to allow  $^2\text{H}$  NMR study of the dynamics of the hydrophobic core of the bilayer. The  $^{31}\text{P}$  spectra of POPC/POPG membranes with varying RTD-1 concentrations are shown in Figure 3a–c. The orientational disorder increased more rapidly with RTD-1 than for the zwitterionic POPC bilayers. At 1.3% RTD-1, the  $90^\circ$  peak is already prominent while the  $0^\circ$  peak shows considerable asymmetric broadening. At 4.0% RTD-1, the  $90^\circ$  peak intensity nearly equals that of the  $0^\circ$  peak, giving rise to a “double horn” line shape. Spectral integration shows that RTD-1 increases the static orientational disorder of POPC/POPG bilayers more than POPC bilayers: the unoriented fraction increases from 38% in the absence of RTD-1 to 73% at 4.0% RTD-1. To gain insight into the type of orientational disorder induced by the peptide, we rotated the alignment axis by  $90^\circ$ . The spectra (Figure 3d–f) exhibit the same chemical shift range as the  $0^\circ$ -aligned samples, indicating that the lipid phase induced by the peptide exhibits no additional fast motion compared to the lamellar bilayer (42).

Since  $^{31}\text{P}$  spectra may be affected by both headgroup conformation and lipid phases, it is important to verify if the changes seen in the  $^{31}\text{P}$  spectra persist in the hydrophobic part of the bilayer.  $^2\text{H}$  NMR is a sensitive probe of the

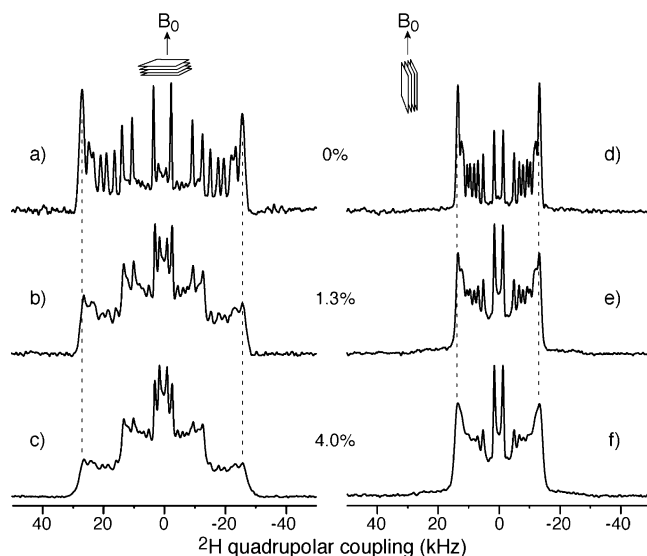


FIGURE 4:  $^2\text{H}$  spectra of oriented POPC/POPG bilayers as a function of RTD-1 concentration: (a and d) 0%, (b and e) 1.3%, and (c and f) 4.0%. The alignment axis was alternately parallel (a–c) and perpendicular (d–f) to  $B_0$ . The  $^2\text{H}$  quadrupolar couplings do not change with the addition of RTD-1, indicating that the dynamics of the hydrophobic core is unaffected by the peptide.

dynamic and static disorder of the hydrophobic core of the bilayer. The  $^2\text{H}$  spectra of POPC- $d_{31}$  mixed with POPG for both the  $0^\circ$  and  $90^\circ$  orientations are shown in Figure 4. The spectra exhibit multiple splittings that correspond to varying  $^2\text{H}$  quadrupolar couplings along the *sn*-2 chain (32, 43, 44). The large splittings result from the groups close to the glycerol backbone, while the smaller splittings originate from the mobile chain ends. In the absence of RTD-1, the  $^2\text{H}$  splittings are well-resolved; upon addition of RTD-1, the resolution deteriorates (Figure 4c), indicating worsening orientation.

The size of the  $^2\text{H}$  quadrupolar couplings ( $\Delta\nu_Q$ ) yields the order parameter of lipid chain motion. In the absence of RTD-1, the largest splitting is  $\sim 52$  kHz while the smallest is  $\sim 5.8$  kHz (Figure 4a). The addition of RTD-1 does not affect these couplings, as the outermost splittings of the spectra remain the same. However, the intensities of the large couplings decreased while those of the small couplings increased (Figure 4c). To verify that the higher intensities at small splittings result from the orientational disorder of the membrane instead of increased mobility, we rotated the glass plates by  $90^\circ$  so that the alignment axis is perpendicular to the magnetic field. At this orientation, the spectral maxima occur at the  $90^\circ$  edge with a frequency of  $P_2(\cos 90^\circ)\Delta\nu_Q = -0.5\Delta\nu_Q$ , which is the same as the maximum peak position of a powder spectrum for a randomly oriented sample. Thus, the size of the splitting when the alignment axis is perpendicular to  $B_0$  is not affected by the degree of static orientational order but only by changes in the lipid chain mobility. The spectra of the  $90^\circ$ -oriented samples in Figure 4d–f clearly show that RTD-1 does not change the coupling strengths but only broadens the line width. Thus, RTD-1 perturbs the orientational order, but not the dynamics of the POPC/POPG bilayer.

Quantitative information about the nature and geometry of the orientational defects of POPC/POPG bilayers induced by RTD-1 can be obtained by simulating the  $^{31}\text{P}$  and  $^2\text{H}$  spectra at 4% RTD-1. To do this, we consider the shape

factors that describe the orientational distribution of the local bilayer normal. For an isotropic powder, the shape factor is  $\sin \beta d\beta$ , where  $\beta$  is the angle between the magnetic field and the bilayer normal. For a 2D planar distribution where the plane is parallel to  $B_0$ , the shape factor is  $d\beta$ . This shape factor results in a symmetric spectrum with equal and maximal intensities at the  $0^\circ$  and  $90^\circ$  frequencies (35, 45). The choice of the possible lipid phases that satisfy the planar distribution for the local bilayer normal orientations is constrained by the observation that the  $^{31}\text{P}$  CSA and  $^2\text{H}$  quadrupolar couplings are not reduced by the peptide, indicating that the lipids do not undergo any fast reorientation other than the uniaxial rotation already present in the lamellar bilayer. The only lipid phase that satisfies both the line shape and the dynamics requirement is a lipid cylinder phase, where the cylinders lie in the plane of the glass plates. Importantly, the local bilayer normals of each cylinder are perpendicular to the cylindrical axis so that these bilayer normals form a 2D planar distribution with respect to  $B_0$ . The cylindrical phase differs from the hexagonal phase in that the cylinders have diameters on the order of micrometers instead of nanometers and are likely multilamellar (see Discussion) so that lateral diffusion of lipids does not narrow the NMR line shape.

The best-fit simulations for the experimental  $^{31}\text{P}$  and  $^2\text{H}$  spectra (Figure 5a,b,d,e) used a model where 99% of the lipids are in the cylindrical phase while 1% of the lipids remain in a lamellar phase with a mosaic spread of  $13^\circ$ . These simulations reproduce well the experimental line shapes for both the  $0^\circ$ - and  $90^\circ$ -oriented samples. In comparison, a model assuming a combination of isotropic orientation distribution and a residual oriented fraction (Figure 5c) disagrees with the experimental spectrum. The best simulation using this model, with 27% oriented fraction and 73% isotropic distribution, shows a much lower intensity near the  $0^\circ$  frequency than the experimental spectrum (Figure 5c).

Simulation of the  $^2\text{H}$  spectra yielded individual quadrupolar couplings, since the line shape is sensitive to small changes in  $\Delta\nu_Q$ . The resulting C–D bond order parameter profile, which is the same with and without RTD-1, is shown in Figure 5f. The profile is similar to that of pure POPC bilayers (44).

We also considered other geometrical models such as toroidal pores in simulating the  $^{31}\text{P}$  and  $^2\text{H}$  line shapes. By considering the pore diameter, thickness, and curvature, we can obtain the shape factors for the torus and calculate the theoretical  $^{31}\text{P}$  line shapes (22). In the absence of motion and with certain geometric parameters, the simulated pore line shapes can fit the experimental spectra. However, the assumptions required to fit the experimental spectra make the pore model unlikely. First, since the pore is confined within each bilayer, and the peptide concentration is low (4%), the radius of the pores must be small, on the order of a few nanometers. Lipid lateral diffusion in these highly curved regions causes fast reorientation, which should average the bilayer  $^{31}\text{P}$  and  $^2\text{H}$  spectra. If this motion is taken into account, then the simulated pore line shape no longer fits the experimental spectrum. In other words, the experimental spectrum is devoid of the motional averaging necessary for nanometer-sized toroidal pores. Second, since pores cannot fill an entire bilayer, only a fraction of the lipids can

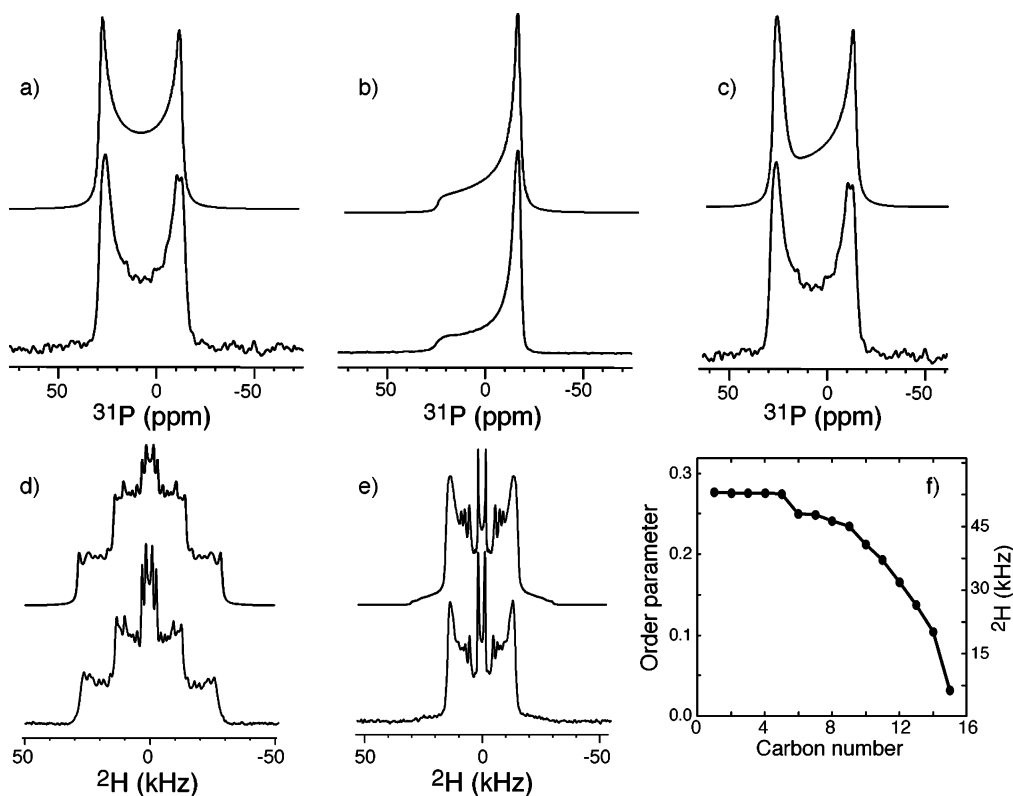


FIGURE 5: Simulated  $^{31}\text{P}$  (a–c) and  $^2\text{H}$  (d and e) spectra of POPC/POPG lipids in the presence of 4% RTD-1. The experimental spectra are reproduced below the simulated spectra for comparison. (a and d) Simulation using a model of 99% bilayer cylinders and 1% residual oriented lipids with a mosaic distribution of  $\pm 13^\circ$  around  $0^\circ$ . The alignment axis is parallel to  $B_0$ . (b and e) Simulation using the same cylinder model as in spectra a and d but with the alignment axis perpendicular to  $B_0$ . (c) Simulated  $^{31}\text{P}$  spectrum using a model of 73% isotropic powder distribution and 27% oriented lipids with a mosaic spread of  $16^\circ$  around  $0^\circ$ . Note the discrepancy between the experimental and simulated line shapes near 20 ppm. The alignment axis is parallel to  $B_0$ . (f)  $^2\text{H}$  order parameter profile for POPC- $d_{31}$  in the presence of POPG and 4.0% RTD-1.

belong to the curved region of the pores; the rest must remain in the lamellar interstices between the pores. Thus, the  $^{31}\text{P}$  spectrum should consist of both an oriented  $0^\circ$  peak for the lamellar lipids and the line shape for the lipids in the curved region of the pores. We found that when a  $0^\circ$  peak is added, the pore line shape even without motion does not fit the experimental spectrum. Last, for the pore geometry to fit the experimental spectrum, we have to assume that all pore axes are aligned with the glass-plate normal. In practice, it is more likely that the pore axes themselves are not well aligned, since the same force that creates the curved walls of the pore can also induce orientational disorder from one bilayer to another. When this interbilayer disorder is taken into account, then the predicted line shape is far more complex and no longer agrees with the experimental spectrum.

To confirm that the lipid cylinders indeed have diameters on the order of micrometers, we measured  $^{31}\text{P}$  2D exchange spectra of the 4% RTD-1–membrane sample. The  $^{31}\text{P}$  chemical shift tensor is sensitive to orientational changes in the lipid molecules. If lateral diffusion over a curved surface within the mixing time of the experiment covers a significant distance, it will induce an orientational change, thus changing the chemical shift. This will manifest as off-diagonal intensities in the 2D spectra. For a cylinder radius of  $1\ \mu\text{m}$ , using a typical lipid lateral diffusion coefficient of  $10^{-8}\ \text{cm}^2/\text{s}$ , significant orientational changes should occur within 200 ms. Motions in this time window can be readily detected by 2D exchange NMR. If the radius is much larger, then in the

same mixing time only diagonal intensities should be observed.

Figure 6a–c shows the 2D exchange spectra of POPC/POPG bilayers with 4% RTD-1, acquired using mixing times of 5, 50, and 400 ms. Up to 50 ms, the spectra remain mostly diagonal, indicating little molecular reorientation. After 400 ms, some off-diagonal intensities are observed. However, between the strong  $0^\circ$  and  $90^\circ$  peaks the cross-peak intensity is still weak. This contrasts with the fully exchanged spectra of unoriented POPC vesicles with a diameter of  $1\ \mu\text{m}$  obtained in our laboratory and shown in the literature (46). Thus, the POPC/POPG cylinders induced by RTD-1 must have diameters of at least  $1\ \mu\text{m}$  for lateral diffusion to be inefficient in causing reorientation.

*Interaction of RTD-1 with Phosphocholine/Cholesterol Membranes.* Since RTD-1 kills microbial cells but is nonhemolytic toward human erythrocytes (26), the question of whether the significant amount of cholesterol present in the mammalian cell membranes protects them against destruction by RTD-1 arises. We prepared POPC/Chol mixtures (1.2:1 molar ratio) with varying RTD-1 concentrations and monitored the bilayer orientational order. The amount of Chol used here mimics the typical cholesterol concentration of  $\sim 25\%$  by mass (equivalent to  $\sim 50\%$  by moles) in erythrocyte membranes (47, 48). The  $^{31}\text{P}$  and  $^2\text{H}$  spectra (Figure 7) show that RTD-1 caused less orientational disorder in POPC/Chol bilayers than in POPC/POPG bilayers. The membrane disorder at 4% RTD-1, averaged over two independently prepared samples, is 51%, compared to

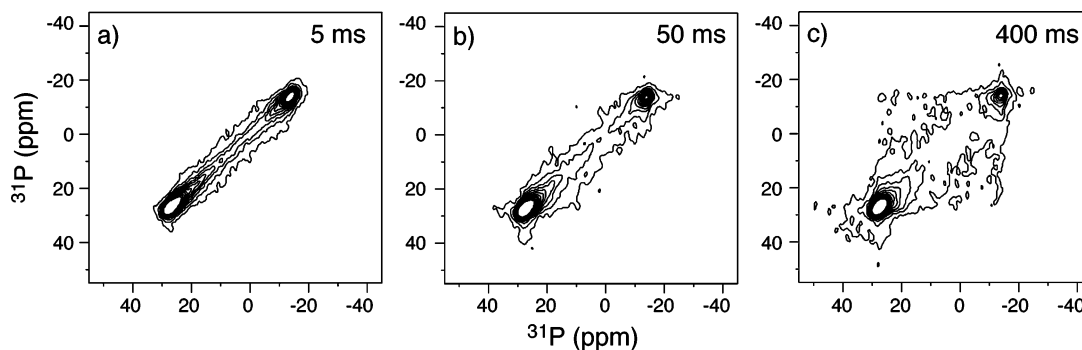


FIGURE 6: 2D  $^{31}\text{P}$  exchange spectra of oriented POPC/POPG lipids with 4% RTD-1, with mixing times of 5 (a), 50 (b), and 400 ms (c). Little off-diagonal intensity is observed between the strong  $0^\circ$  and  $90^\circ$  peaks even with the longest mixing time, indicating that the bilayer cylinders are sufficiently large that lipid lateral diffusion does not cause large-angle reorientations within 400 ms.

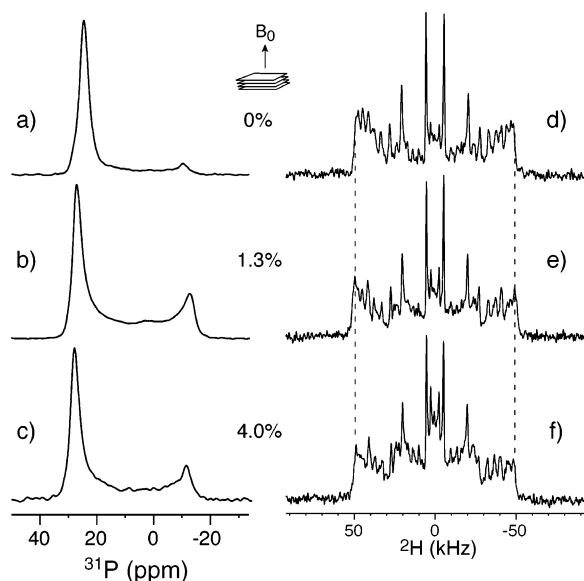


FIGURE 7:  $^{31}\text{P}$  (a–c) and  $^2\text{H}$  (d–f) spectra of POPC/Chol (1.2:1) bilayers with 0% (a and d), 1.3% (b and e), and 4.0% (c and f) RTD-1. The orientational disorder created by the peptide is more moderate than that in POPC/POPG bilayers. The peptide concentration is calculated using the total mole amount of POPC and Chol. If normalized relative to POPC, the peptide concentrations are 0%, 2.4%, and 7.3%. Spectra a–c and d–f correspond to two independent series of samples to illustrate experimental uncertainties in the extent of membrane alignment. The disorder in Figure 8 is obtained from the average of these measurements.

72% for the POPC/POPG sample. Consistently, the  $^2\text{H}$  spectra show less orientational broadening than the corresponding POPC/POPG samples.

The ability of cholesterol to attenuate the destabilizing effect of RTD-1 is particularly striking if one takes into account the fact that the peptide concentrations were calculated using the sum of POPC and cholesterol molar quantity. Since POPC is the only bilayer-forming lipid, it can be argued that the actual RTD-1 concentration should be calculated relative to POPC alone, and is thus a factor of  $\sim 2$  higher than the reported values. With this alternative criterion, the RTD-1 concentrations that are used are 2.4 and 7.3%, much higher than for POPC/POPG mixtures. Even at these elevated concentrations, the orientational disorder of the membrane is smaller than that of the anionic bilayer mixture.

A major difference between the  $^2\text{H}$  spectra of the POPC/Chol series and those of the POPC/POPG series is the increase of the quadrupolar couplings by a factor of nearly

2. For example, the largest splitting of the POPC/Chol spectra is 97 kHz, while the largest  $^2\text{H}$  splitting in the POPC/POPG bilayer is 52 kHz. The increased  $^2\text{H}$  order parameters reflect the reduced mobility of the lipid acyl chains, which is known to result from the packing of cholesterol in the hydrophobic part of the bilayer (49).

Figure 8 compares the RTD-1-induced orientational disorder of the three lipid membranes: POPC, POPC/POPG, and POPC/Chol. The left graph shows the percent disorder as a function of peptide concentration. RTD-1 causes the greatest orientational disorder in POPC/POPG bilayers, followed by POPC/Chol and then POPC bilayers. Since the disorder in the peptide-free samples differs for the three membranes due to the inherent differences in the ability of lipids to align, we also show the fractional increase in disorder as a function of peptide concentration for each series (Figure 8b). This is obtained by normalizing the percent disorder relative to that of the 0% sample in each membrane series. Using this criterion, the POPC/POPG bilayer remains the most vulnerable to perturbation by RTD-1, while POPC and POPC/Chol mixtures increase the disorder more slowly; the trend appears to taper off above 1.3%.

*Motion and Orientation of RTD-1 in Phosphocholine Bilayers.* The results described above concern the interaction of RTD-1 with lipid bilayers with various compositions. To obtain information about the dynamic structure of RTD-1 itself in the membrane, we conducted MAS experiments on both lipid-free and lipid-bound RTD-1. The peptide was labeled with  $^{13}\text{C}$  at Leu-6 and with  $^{15}\text{N}$  at Cys-7. The  $^{13}\text{C}$  and  $^{15}\text{N}$  MAS spectra were recorded at a slow spinning speed of 1.8 kHz to yield sufficient spinning sidebands from which chemical shift anisotropies could be determined. DLPC was used as the lipid matrix because this short chain lipid was previously shown to best accommodate PG-1 binding and to allow fast uniaxial rotation of PG-1 (8, 10).

Figure 9 shows the lipid-free and lipid-bound RTD-1 spectra under MAS for  $^{13}\text{C}$ -labeled L6 and  $^{15}\text{N}$ -labeled C7. Interestingly, the membrane-bound peptide, similar to the pure peptide, gives significant sideband intensities indicative of rigid-limit anisotropies. Hertzfeld–Berger analysis of the  $^{15}\text{N}$  sideband manifold yielded an anisotropy  $\delta_{\text{N}}$  of 100.4 ppm and an asymmetry parameter  $\eta_{\text{N}}$  of 0.11 for the pure RTD-1, while the membrane-bound RTD-1 has a  $\delta_{\text{N}}$  of 98.3 ppm and an  $\eta_{\text{N}}$  of 0.01. The  $^{13}\text{C}$  chemical shift tensor of pure RTD-1 has a  $\delta_{\text{C}}$  of  $-81.5$  ppm, an  $\eta_{\text{C}}$  of 0.80, and an isotropic shift of 173.8 ppm (relative to TMS). The random coil isotropic shift of the carbonyl of Leu was reported to

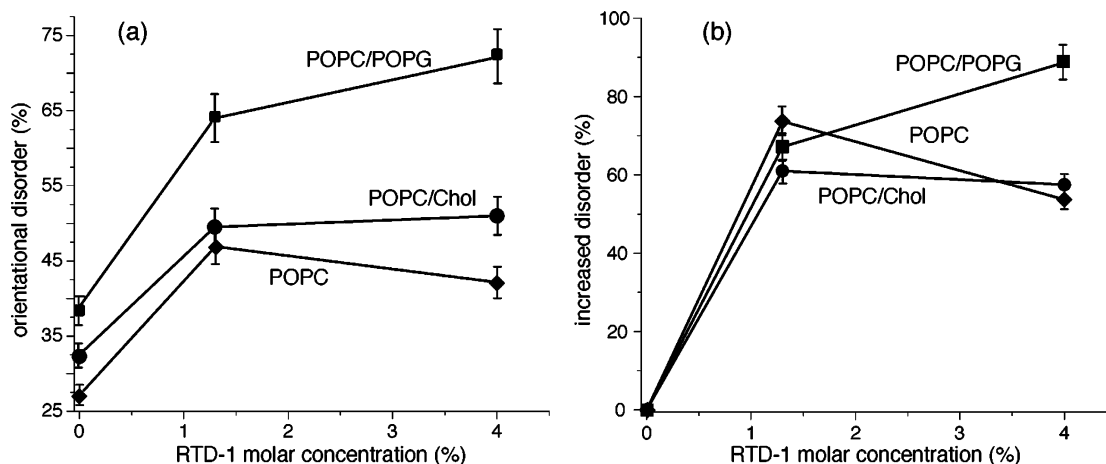


FIGURE 8: Comparison of the orientational disorder induced by RTD-1 for different membrane compositions. (a) Disorder of POPC/POPG (■), POPC/cholesterol (●), and POPC (◆) bilayers, calculated as the fraction of the intensity outside the  $0^\circ$  peak relative to the whole spectra. (b) Relative disorder, obtained as the normalized difference with respect to the 0% sample in each membrane series.

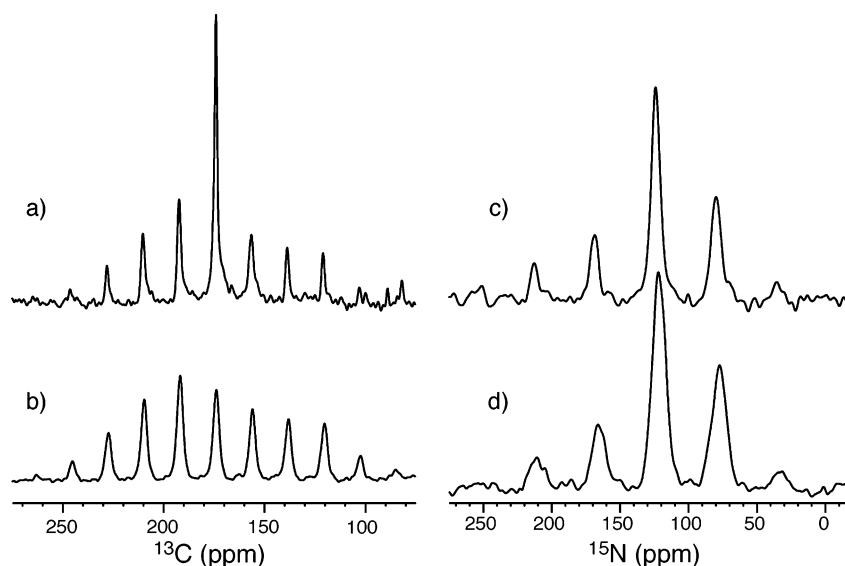


FIGURE 9:  $^{13}\text{C}$  (a and b) and  $^{15}\text{N}$  (c and d) MAS spectra of L6  $^{13}\text{C}$ - and C7  $^{15}\text{N}$ -labeled RTD-1 at a spinning speed of 1.8 kHz. (a and c) RTD-1 bound to DLPC lipids. (b and d) Lipid-free RTD-1. Note the narrower line widths of the membrane-bound RTD-1. The number of scans is  $\sim 25000$  for the membrane-bound peptide (a and c) and 1000–3000 for the lipid-free peptide (b and d).

be 177.6 ppm relative to DSS, which translates to 175.9 ppm on the TMS scale (50, 51). Thus, the chemical shift of  $^{13}\text{C}$ -labeled L6 is consistent with a strong  $\beta$ -sheet conformation. Unfortunately, the  $^{13}\text{C}$ -labeled CSA of the membrane-bound RTD-1 cannot be obtained because of the overlap between the L6 center band and the lipid  $^{13}\text{C}$  signals. However, the sideband intensity distribution, which is not obscured by the lipid carbonyl peak due to the latter's small CSA, is almost identical with the sideband envelope of unbound RTD-1. This confirms the  $^{15}\text{N}$  result that RTD-1 is immobilized in the membrane.

Two possibilities account for the lack of large-amplitude motion of RTD-1 in the membrane. One is that the peptide aggregates in the DLPC bilayer. If so, the aggregate must be well-ordered since both the  $^{13}\text{C}$  and  $^{15}\text{N}$  line widths are narrow. The  $^{15}\text{N}$  fwhms decrease from 11.7 to 8.0 ppm, while the  $^{13}\text{C}$  line widths decrease from 3.4 to 2.0 ppm. The reduced line widths indicate that the  $\beta$ -sheet structure of the peptide becomes more ordered after binding to the membrane. The second scenario is that the peptide is trapped in small membrane defects and cannot rotate. More extensive

structural characterization needs to be carried out to identify the exact molecular origin of this immobilization. It is interesting to note that in aqueous solution RTD-1 shows significant internal flexibility (25) despite the ladder structure imposed by the three disulfide bonds.

To determine the orientation of RTD-1 in the lipid bilayer, we measured the  $^{13}\text{C}$ -labeled L6 and  $^{15}\text{N}$ -labeled C7 anisotropic chemical shifts in uniaxially aligned DLPC bilayers. The orientation of a  $\beta$ -sheet peptide can be specified in terms of its strand axis direction and its sheet plane orientation. The  $^{13}\text{C}$  chemical shift tensor has its most downfield axis ( $\sigma_{11}$ ) parallel to the strand axis and its most upfield axis ( $\sigma_{33}$ ) perpendicular to the  $\beta$ -sheet plane. The  $^{15}\text{N}$  chemical shift tensor complements this, since the main  $^{15}\text{N}$  principal axis is roughly perpendicular to the strand axis.

Figure 10 shows the static  $^{13}\text{C}$  and  $^{15}\text{N}$  spectra of RTD-1 oriented in DLPC bilayers. The two sharp signals at 193 and 174 ppm are the lipid carbonyl peaks. The  $^{13}\text{C}$ -labeled L6 signal shows a distribution of frequencies between 170 and 230 ppm and forms a broad base below the two sharp lipid signals. Consistently, the chemical shift of  $^{15}\text{N}$ -labeled C7

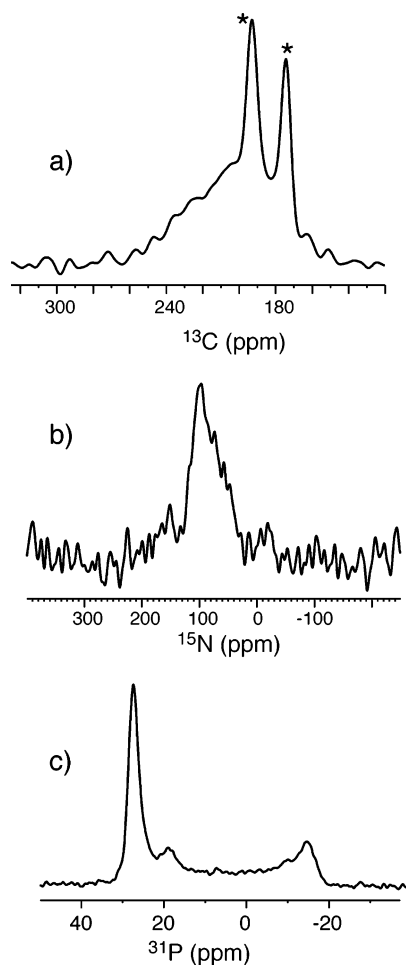


FIGURE 10:  $^{13}\text{C}$  (a) and  $^{15}\text{N}$  (b) static spectra of L6  $^{13}\text{C}$ O- and C7  $^{15}\text{N}$ -labeled RTD-1 in oriented DLPC bilayers. (c)  $^{31}\text{P}$  spectrum of the lipid membrane at the end of the  $^{13}\text{C}$  and  $^{15}\text{N}$  measurements. Asterisks in panel a denote the lipid carbonyl signals, which partially overlap with the L6  $^{13}\text{C}$ O peak. The broad  $^{13}\text{C}$  and  $^{15}\text{N}$  peaks indicate orientation distribution. The number of scans is  $\sim 30000$  for spectrum a and  $\sim 65000$  for spectrum b.

ranges from 50 to 120 ppm with the maximum at 100 ppm. Thus, RTD-1 does not adopt a unique orientation with respect to the magnetic field. To obtain more quantitative information about the orientation distribution, we calculated the  $^{13}\text{C}$ O and  $^{15}\text{N}$  anisotropic chemical shifts for different peptide orientations. Figure 11 shows the 2D orientational plot where the contour levels represent the measured  $^{13}\text{C}$  (170–230 ppm) and  $^{15}\text{N}$  (50–120 ppm) anisotropic shifts and the axes define the polar coordinates ( $\alpha, \beta$ ) of  $B_0$  in the PDB frame of the peptide. Structure 18 of RTD-1 was used to obtain this orientational plot; however, two more structures were also used to calculate the peptide orientation, and similar results were obtained. It can be seen that the overlap between the  $^{13}\text{C}$  (dashed lines) and  $^{15}\text{N}$  (solid lines) contours defines not a specific point but a region in the angular space, indicating that a distribution of orientations is allowed. To illustrate the orientational distribution, we selected three points in the contour plot corresponding to the maximum peak positions of the  $^{13}\text{C}$  ( $200 \pm 10$  ppm) and  $^{15}\text{N}$  ( $100 \pm 10$  ppm) spectra. These orientations are shown in Figure 11b; two of these are tilted from the magnetic field, while the third is horizontal.

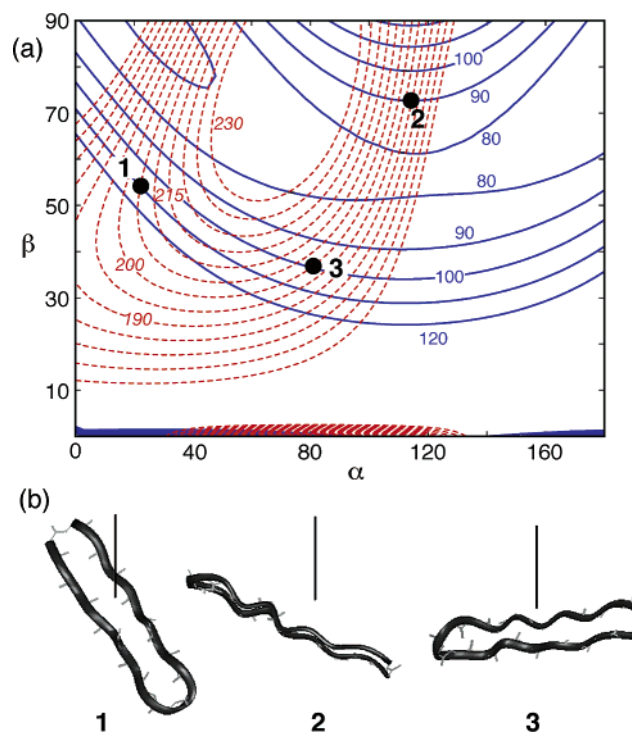


FIGURE 11: Orientation of RTD-1 based on  $^{13}\text{C}$  and  $^{15}\text{N}$  anisotropic chemical shifts. (a) Calculated L6  $^{13}\text{C}$ O (dashed red lines) and C7  $^{15}\text{N}$  (solid blue lines) chemical shifts as a function of the polar angle  $\beta$  and azimuthal angle  $\alpha$  of  $B_0$  in the molecular frame of the peptide defined by the PDB structure of RTD-1. (b) RTD-1 orientations corresponding to the three indicated positions in the contour plot. The vertical line in each structure represents the  $B_0$  direction, which coincides with the bilayer normal in the case of perfect alignment.

It is interesting to note that the broad  $^{15}\text{N}$  peak of RTD-1 centered at 100 ppm resembles the spectra of several  $\alpha$ -helical frog-derived antimicrobial peptides of Australian tree frogs (52). Since the N–H bonds in helical peptides are roughly parallel to the helical axis, the observation of a broad peak close to the  $^{15}\text{N}$  isotropic chemical shift suggests that the helix axis is near the magic angle from the membrane normal. In contrast, in a  $\beta$ -sheet peptide such as RTD-1, the  $^{15}\text{N}$  chemical shift principal axis is approximately perpendicular to the  $\beta$ -strand axis. Thus, the orientation of the peptide differs from that in the helical case. Without additional  $^{13}\text{C}$ O chemical shift restraints, no unique  $\beta$ -sheet orientation can be extracted from the  $^{15}\text{N}$  chemical shift alone, even if a narrow anisotropic frequency is measured.

## DISCUSSION

*Lipid Cylinder Model of RTD-1–Membrane Interactions.* The goal of this work is to investigate if RTD-1 interacts preferentially with lipid bilayers of different compositions to gain insight into the antimicrobial selectivity of this peptide. The zwitterionic POPC bilayer serves as a reference system, while the mixed POPC/Chol bilayer mimics the eukaryotic cell membrane and the anionic POPC/POPG bilayer the bacterial cell membrane. For each bilayer system, the RTD-1 concentration was varied. The peptide-free bilayer samples (0%) act as controls to account for the differences in the ease of aligning the membrane so that comparisons can be made about the extent of disorder created by RTD-1.

We found that in zwitterionic PC membranes both with and without cholesterol, RTD-1 causes moderate disordering

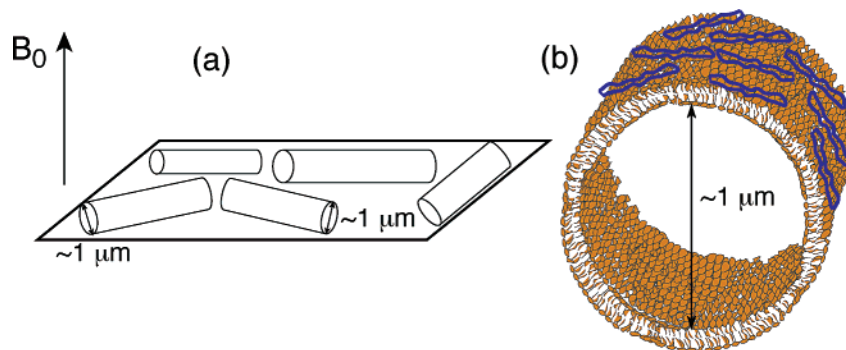


FIGURE 12: Model of lipid cylinder formation in POPC/POPG membranes due to RTD-1 binding. (a) Visualization of the cylinders on glass plates. (b) Visualization of each cylinder with a diameter on the order of a few micrometers. For simplicity, only one bilayer is drawn, but the cylinders are most likely multilamellar. For clarity, the bilayer thickness and the cylindrical diameter are not drawn to scale. RTD-1 most likely binds to the outer leaflet of the membrane in an asymmetric fashion, which causes a weak curvature that makes the bilayer fold onto itself to form the cylinder.

of the bilayer structure. The spectra (Figures 1 and 7) are dominated by the  $0^\circ$  frequency peak, and significant resolution remains in the  $^2\text{H}$  spectra. The disordered intensity is mainly manifested as the  $90^\circ$  frequency peak (Figure 7d–f). The line shape of the disordered intensity in these spectra resembles that of the POPC/POPG spectrum with 4% RTD-1 (Figure 3c) but at much lower levels. This suggests that the weak orientational disorder induced by RTD-1 in zwitterionic membranes is similar to the disorder formed more drastically in the anionic membranes. Interestingly, the interaction of RTD-1 with PC membranes does not depend on the bilayer thickness (Figure 2), in clear contrast to PG-1 (8). This suggests that RTD-1 does not insert into PC bilayers.

Compared to zwitterionic bilayers, the POPC/POPG bilayers with 25% negative surface charges exhibit more significant orientational disorder upon RTD-1 binding. The  $^{31}\text{P}$  spectrum of the 4% RTD-1 sample exhibits a symmetric line shape that differs markedly from both the perfect  $0^\circ$ -oriented spectrum and the isotropic powder spectrum. This preferential destabilization of the orientational order of the anionic bilayer over the zwitterionic bilayers indicates that electrostatic attraction between the cationic RTD-1 and the anionic bilayer is crucial to membrane disruption. Thus, the selectivity of RTD-1 against bacterial membranes rich in anionic lipids may be primarily a result of this favorable electrostatic interaction.

Simulations of the POPC/POPG spectra provided useful insight into the type of lipid phases caused by RTD-1. Using a macroscopic bilayer cylinder model, in which the cylindrical axes lie in the plane of the glass plates (Figure 12a), we reproduced the experimental  $^{31}\text{P}$  and  $^2\text{H}$  spectra for both the  $0^\circ$  and  $90^\circ$  alignment directions (spectra a and b of Figure 5, respectively). When the glass-plate alignment axis is parallel to  $B_0$ , the local bilayer normals, which are perpendicular to the cylinder axis, form a 2D planar distribution with respect to  $B_0$ . The observed symmetric line shape is uniquely fit by this planar distribution in the static limit. An alternative model combining isotropic orientation distribution with a residual  $0^\circ$ -aligned component cannot reproduce the symmetric line shape (Figure 5c). Thus, the membrane disorder created by RTD-1 cannot be described as a random orientation distribution.

The lipid cylinders are likely multilamellar and may have water in the center (Figure 12b). The average length of these cylinders is not known, but it should be sufficiently long

for the lipids at the end caps with different orientations not to make a significant contribution to the spectra. The lipid cylinders must have relatively large diameters of a few micrometers, to prevent lipid lateral diffusion from causing reorientations fast on the  $^{31}\text{P}$  chemical shift time scale. It is well-known that in the inverted hexagonal phase, where the cylindrical rods have a diameter of only two lipid molecules ( $\sim 5$  nm), the lateral diffusion of the lipids over the curved surface causes fast averaging of the NMR spectra. In this case, since the axis of the lateral diffusion, the cylindrical axis, is perpendicular to the bilayer normals, the NMR frequencies are scaled by  $P_2(\cos 90^\circ) = -0.5$ . Thus, the  $^{31}\text{P}$  spectra of hexagonal-phase lipids are halved and mirror-imaged from the lamellar bilayer spectra (42). We did not observe fast motional averaging of the  $^{31}\text{P}$  and  $^2\text{H}$  spectra for the POPC/POPG lipids with 4% RTD-1. Combined with the 2D exchange results, this means that the correlation time ( $\tau$ ) for laterally induced lipid reorientation is at least 100 ms. On the basis of the typical lipid lateral diffusion coefficients (46) and the relation  $D = \langle r^2 \rangle / 6\tau$ , we estimate that the minimum root-mean-square radius of the lipid cylinder is  $0.8\text{--}2.4 \mu\text{m}$ .

How does RTD-1 bind to this anionic lipid cylinder? If we make the reasonable assumption that the chain length independence of the interaction of RTD-1 with PC bilayers also holds true for POPC/POPG bilayers, then RTD-1 most likely binds to the headgroup region of the POPC/POPG membrane (Figure 12b). This surface binding has to be sufficiently shallow; otherwise, the membrane would be laterally expanded and the acyl chains would experience additional motional averaging (32), which is not detected in the  $^2\text{H}$  spectra (Figure 4). This surface binding model is supported by previous oriented circular dichroism and X-ray diffraction results on this peptide (12).

How does RTD-1 induce cylinder formation? We hypothesize that RTD-1 binds asymmetrically to the POPC/POPG bilayer, primarily on the outer leaflet, so that it causes a bilayer curvature, forcing the bilayer to fold onto itself to form a large cylinder. Transbilayer asymmetry has been documented to change the morphology of lipid vesicles into long cylinders. For example, when DOPG is preferentially transported from the inner to the outer monolayer of large unilamellar vesicles composed of DOPC and DOPG, long tubules were observed by cryoelectron microscopy (53). The insertion of monooleoylphosphocholine into the outer mono-

layer also resulted in tubules (53). Peptide-induced lipid tubule formation has also been reported before, for example, for a *de novo*-designed 18-residue amphipathic helical peptide (54) and for gramicidin D (36). Cylindrical lipid phases are also found *in vivo*, triggered by proteins that aggregate into a coat scaffold on the membrane surface and impose a curvature (55). Such tubules play an important role in the intracellular trafficking between organelles and between organelles and the plasma membrane. A different type of lipid tubule, with diameters of  $\sim 0.5 \mu\text{m}$  and lengths of 50–200  $\mu\text{m}$ , has been observed to form from phospholipids containing diacetylenic acyl chains (56–59). In this case, the mechanism of tubule formation is chiral packing of neighboring lipid molecules. Finally, equilibrium among bilayer cylinders and vesicles was reported in surfactant mixtures (60). A common framework with which to understand the tubule morphology is the elastic bending energy theory of the bilayer. In this theory, the surface area difference between the two monolayers creates the bending force while membrane elastic constants and spontaneous curvature control the precise topology of the nonspherical structure (61, 62).

The reduced amount of the lipid tubule phase in the zwitterionic membranes probably results from the weaker binding of the peptide to these neutral membranes. For the POPC/Chol mixture, another possible mechanism for the attenuated membrane-destabilizing effect of RTD-1 is the well-known insertion of cholesterol into the hydrophobic center of the bilayer (63). This insertion may counter the RTD-1-induced positive curvature strain of the membrane, thus delaying the onset of lipid cylinders.

$^{13}\text{C}$  and  $^{15}\text{N}$  chemical shifts of uniaxially aligned RTD-1 indicate that RTD-1 adopts a distribution of orientations. The  $^{13}\text{C}$  and  $^{15}\text{N}$  spectra (Figure 10a,b) show broad patterns that deviate from the powder patterns of a random orientation distribution. Both tilted and horizontal RTD-1 orientations are found relative to the magnetic field (Figure 11b). The most likely cause for this orientational distribution is the residual alignment disorder of the bilayers. The  $^{31}\text{P}$  spectrum of the glass-plate sample (Figure 10c) exhibits a low level of unoriented intensities between 25 and  $-15$  ppm that is reminiscent of the 2D planar distribution seen in the POPC/POPG spectrum (Figure 3c). This residual disorder likely corresponds to a small fraction of lipid cylinders so that as the bilayer curls the peptide orientation relative to the magnetic field also changes. Further attempts to orient the membrane in the presence of the peptide did not significantly improve the alignment. Since the function of RTD-1 is to destroy the membrane structure, this is not surprising. Another possibility for the orientation distribution is that RTD-1 molecules aggregate with a certain twist angle between neighboring molecules so that even with the same bilayer normal direction, the peptide orientation may vary. Such twisting is not unusual for the  $\beta$ -sheet structure, as it is the basis for the formation of  $\beta$ -barrel proteins (64). Since RTD-1 shows rigid-limit chemical shift anisotropies in the membrane (Figure 9), no intermediate time scale motion can contribute to the  $^{13}\text{C}$  and  $^{15}\text{N}$  frequency distribution. The low intensity at 18 ppm in the  $^{31}\text{P}$  spectrum (Figure 10c) is attributed to small conformational changes of some of the lipid headgroups induced by the peptide, since its frequency does not correspond to any known lipid phases.

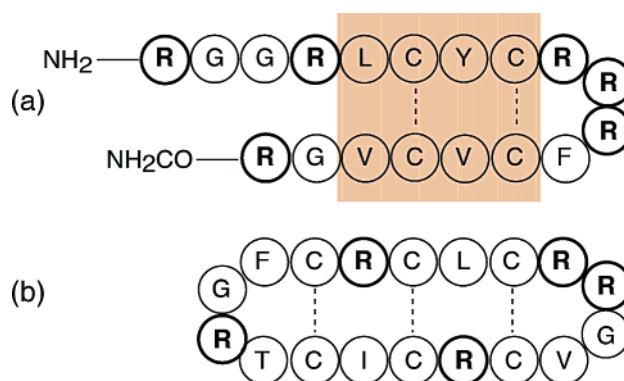


FIGURE 13: Amino acid sequences of (a) PG-1 and (b) RTD-1. Note the different distributions of Arg and the presence of a hydrophobic patch (shaded area) in PG-1.

**Difference between RTD-1 and PG-1.** RTD-1 resembles PG-1 in both primary and secondary structures (Figure 13). Both are 18-residue  $\beta$ -hairpin peptides, have multiple disulfide bonds that link the two strands of the turn, and have five or six Arg residues. The differences are the cyclic nature of RTD-1 versus the open chain of PG-1 and the distributions of Arg residues. In PG-1, the six Arg residues are clustered at the two ends of the  $\beta$ -hairpin, making it an amphipathic molecule, while in RTD-1, the five Arg residues are spread throughout the molecule (Figure 13).

The solid-state NMR study presented here shows that RTD-1 interacts with the lipid bilayer in a fashion strikingly different from that of PG-1. PG-1 perturbs PC bilayers according to the bilayer thickness, while binding of RTD-1 to the membrane does not depend on the acyl chain length. PG-1 completely destroys the POPC bilayer orientation, whereas RTD-1 retains much of the structural order. PG-1 rotates uniaxially in DLPC bilayers, while RTD-1 is immobilized. PG-1 inserts completely into DLPC bilayers in a tilted fashion, while RTD-1 most likely binds to the membrane surface. RTD-1 causes the formation of lipid cylinders in POPC/POPG membranes, whereas PG-1 breaks the POPC/POPG membrane into small vesicles with intermediate time scale motions (unpublished results). While the interaction of PG-1 with membranes is readily correlated with bilayer disruption, the mode of interaction of RTD-1 with anionic membranes, cylinder formation, seems to be a more subtle way of affecting bilayer structural integrity. More studies need to be carried out to elucidate how cylinder formation by RTD-1 leads to eventual membrane rupture. Overall, the NMR data indicate that RTD-1 has a more moderate effect on membrane integrity than PG-1. This conclusion is consistent with the known weaker antimicrobial activity of RTD-1 compared to PG-1 (26). It is also in good agreement with a recent diffraction and circular dichroism study, which found that a much higher concentration of RTD-1 is required to cause membrane thinning, and that RTD-1 cannot insert into fully hydrated membranes even at high concentrations (12).

We hypothesize that these differences between RTD-1 and PG-1 mainly result from the lack of amphiphilic character of RTD-1 (25). Unlike the case with PG-1, there is not a contiguous and significant hydrophobic patch in RTD-1 to allow it to insert into the lipid bilayer strongly. This study shows that anionic lipids are required for RTD-1 to bind strongly to the membrane. Once bound, it appears that RTD-1

inserts sufficiently into the bilayer to cause a weak curvature such that the bilayer folds into micrometer-diameter cylinders; however, the insertion is not beyond the glycerol region since chain mobility is unaffected, as indicated by the  $^2\text{H}$  spectra (Figure 4). This distinct mode of interaction of RTD-1 with the membrane underscores the functional diversity of antimicrobial peptides caused by subtle sequence changes.

## ACKNOWLEDGMENT

We thank Teresa Hong for assistance in RTD-1 synthesis.

## REFERENCES

- Kokryakov, V. N., Harwig, S. S., Panyutich, E. A., Shevchenko, A. A., Aleshina, G. M., Shamova, O. V., Korneva, H. A., and Lehrer, R. I. (1993) Protegrins: leukocyte antimicrobial peptides that combine features of corticostatic defensins and tachyplesins, *FEBS Lett.* **327**, 231–236.
- Nakamura, T., Furunaka, H., Miyata, T., Tokunaga, F., Muta, T., Iwanaga, S., Niwa, M., Takao, T., and Shimonishi, Y. (1988) Tachyplesin, a class of antimicrobial peptide from the hemocytes of the horseshoe crab (*Tachyplesus tridentatus*). Isolation and chemical structure, *J. Biol. Chem.* **263**, 16709–16713.
- Lehrer, R. I., Lichtenstein, A. K., and Ganz, T. (1993) Defensins: antimicrobial and cytotoxic peptides at mammalian cells, *Annu. Rev. Immunol.* **11**, 105–128.
- van't Hof, W., Veerman, E. C., Helmerhorst, E. J., and Amerongen, A. V. (2001) Antimicrobial peptides: properties and applicability, *Biol. Chem.* **382**, 597–619.
- Scott, M. G., and Hancock, R. E. (2000) Cationic antimicrobial peptides and their multifunctional role in the immune system, *Crit. Rev. Immunol.* **20**, 407–431.
- Hancock, R. E., and Lehrer, R. (1998) Cationic peptides: a new source of antibiotics, *Trends Biotechnol.* **16**, 82–88.
- Matsuzaki, K. (1998) Magainins as paradigm for the mode of action of pore forming polypeptides, *Biochim. Biophys. Acta* **1376**, 391–400.
- Yamaguchi, S., Hong, T., Waring, A., Lehrer, R. I., and Hong, M. (2002) Solid-state NMR investigations of peptide-lipid interaction and orientation of a  $\beta$ -sheet antimicrobial peptide, protegrin, *Biochemistry* **41**, 9852–9862.
- Buffy, J., Hong, T., Yamaguchi, S., Waring, A., Lehrer, R., and Hong, M. (2003) Solid-State NMR Investigation of the Depth of Insertion of Protegrin-1 in Lipid Bilayers Using Paramagnetic  $\text{Mn}^{2+}$ , *Biophys. J.* **85**, 1–11.
- Buffy, J. J., Waring, A. J., Lehrer, R. I., and Hong, M. (2003) Immobilization and Aggregation of Antimicrobial Peptide Protegrin in Lipid Bilayers Investigated by Solid-State NMR, *Biochemistry* **42**, 13725–13734.
- Laederach, A., Andreotti, A. H., and Fulton, D. B. (2002) Solution and micelle-bound structures of tachyplesin I and its active aromatic linear derivatives, *Biochemistry* **41**, 12359–12368.
- Weiss, T. M., Yang, L., Ding, L., Waring, A. J., Lehrer, R. I., and Huang, H. W. (2002) Two states of cyclic antimicrobial peptide RTD-1 in lipid bilayers, *Biochemistry* **41**, 10070–10076.
- Bechinger, B. (1999) The structure, dynamics, and orientation of antimicrobial peptides in membranes by multidimensional solid-state NMR spectroscopy, *Biochim. Biophys. Acta* **1462**, 157–183.
- Pouny, Y., Rapaport, D., Mor, A., Nicolas, P., and Shai, Y. (1992) Interaction of antimicrobial dermaseptin and its fluorescently labeled analogues with phospholipid membranes, *Biochemistry* **31**, 12416–12423.
- Bechinger, B., Zasloff, M., and Opella, S. J. (1993) Structure and orientation of the antibiotic peptide magainin in membranes by solid-state nuclear magnetic resonance spectroscopy, *Protein Sci.* **2**, 2077–2084.
- Bechinger, B., Zasloff, M., and Opella, S. J. (1998) Structure and dynamics of the antibiotic peptide PGLa in membranes by solution and solid-state nuclear magnetic resonance spectroscopy, *Biophys. J.* **74**, 981–987.
- Marassi, F. M., Opella, S. J., Juvvadi, P., and Merrifield, R. B. (1999) Orientation of cecropin A helices in phospholipid bilayers determined by solid-state NMR spectroscopy, *Biophys. J.* **77**, 3152–3155.
- He, K., Ludtke, S. J., Huang, H. W., and Worcester, D. L. (1995) Antimicrobial peptide pores in membranes detected by neutron in-plane scattering, *Biochemistry* **34**, 15614–15618.
- He, K., Ludtke, S. J., Heller, W. T., and Huang, H. W. (1996) Mechanism of alamethicin insertion into lipid bilayers, *Biophys. J.* **71**, 2669–2679.
- Ludtke, S. J., He, K., Heller, W. T., Harroun, T. A., Yang, L., and Huang, H. W. (1996) Membrane pores induced by magainin, *Biochemistry* **35**, 13723–13728.
- Yang, L., Weiss, T. M., Lehrer, R. I., and Huang, H. W. (2000) Crystallization of antimicrobial pores in membranes: magainin and protegrin, *Biophys. J.* **79**, 2002–2009.
- Hallock, K. J., Lee, D. K., and Ramamoorthy, A. (2003) MSI-78, an Analogue of the Magainin Antimicrobial Peptides, Disrupts Lipid Bilayer Structure via Positive Curvature Strain, *Biophys. J.* **84**, 3052–3060.
- Tang, Y. Q., Yuan, J., Osapay, G., Osapay, K., Tran, D., Miller, C. J., Ouellette, A. J., and Selsted, M. E. (1999) A cyclic antimicrobial peptide produced in primate leukocytes by the ligation of two truncated  $\alpha$ -defensins, *Science* **286**, 498–502.
- Tran, D., Tran, P. A., Tang, Y. Q., Yuan, J., Cole, T., and Selsted, M. E. (2002) Homodimeric  $\theta$ -defensins from rhesus macaque leukocytes: isolation, synthesis, antimicrobial activities, and bacterial binding properties of the cyclic peptides, *J. Biol. Chem.* **277**, 3079–3084.
- Trabi, M., Schirra, H. J., and Craik, D. J. (2001) Three-dimensional structure of RTD-1, a cyclic antimicrobial defensin from rhesus macaque leukocytes, *Biochemistry* **40**, 4211–4221.
- Tam, J. P., Lu, Y. A., and Yang, J. L. (2000) Marked increase in membranolytic selectivity of novel cyclic tachyplesins constrained with an antiparallel two- $\beta$ -strand cystine knot framework, *Biochem. Biophys. Res. Commun.* **267**, 783–790.
- Tam, J. P., Wu, C., and Yang, J. L. (2000) Membranolytic selectivity of cystine-stabilized cyclic protegrins, *Eur. J. Biochem.* **267**, 3289–3300.
- Davis, J. H., and Auger, M. (1999) Static and magic angle spinning NMR of membrane peptides and proteins, *Prog. NMR Spectrosc.* **35**, 1–84.
- Marassi, F. M., and Opella, S. J. (1998) NMR structural studies of membrane proteins, *Curr. Opin. Struct. Biol.* **8**, 640–648.
- Heller, W. T., Waring, A. J., Lehrer, R. I., and Huang, H. W. (1998) Multiple states of  $\beta$ -sheet peptide protegrin in lipid bilayers, *Biochemistry* **37**, 17331–17338.
- Hallock, K. J., Henzler Wildman, K., Lee, D. K., and Ramamoorthy, A. (2002) An innovative procedure using a sublimable solid to align lipid bilayers for solid-state NMR studies, *Biophys. J.* **82**, 2499–2503.
- Yamaguchi, S., Huster, D., Waring, A., Lehrer, R. I., Kearney, W., Tack, B. F., and Hong, M. (2001) Orientation and dynamics of an antimicrobial peptide in the lipid bilayer by solid-state NMR spectroscopy, *Biophys. J.* **81**, 2203–2214.
- Jeener, J., Meier, B. H., Bachmann, P., and Ernst, R. R. (1979) Investigation of exchange processes by two-dimensional NMR spectroscopy, *J. Chem. Phys.* **71**, 4546–4554.
- Mehring, M. (1983) *High-Resolution NMR in Solids*, Springer-Verlag, New York.
- Schmidt-Rohr, K., and Spiess, H. W. (1994) *Multidimensional Solid-State NMR and Polymers*, Academic Press, San Diego.
- Moll, F., III, and Cross, T. A. (1990) Optimizing and characterizing alignment of oriented lipid bilayers containing gramicidin D, *Biophys. J.* **57**, 351–362.
- Hartzell, C. J., Whitfield, M., Oas, T. G., and Drobny, G. P. (1987) Determination of the  $^{15}\text{N}$  and  $^{13}\text{C}$  chemical shift tensors of L-[ $^{13}\text{C}$ ]-alanyl-L-[ $^{15}\text{N}$ ]alanine from the dipole-coupled powder patterns, *J. Am. Chem. Soc.* **109**, 5966–5969.
- Separovic, F., Smith, R., Yannoni, C. S., and Cornell, B. A. (1990) Molecular sequence effects on the  $^{13}\text{C}$  carbonyl chemical shift shielding tensor, *J. Am. Chem. Soc.* **112**, 8324–8328.
- Wu, C. H., Ramamoorthy, A., Gierasch, L. M., and Opella, S. J. (1995) Simultaneous characterization of the amide  $^1\text{H}$  chemical shift,  $^1\text{H}$ - $^{15}\text{N}$  dipolar, and  $^{15}\text{N}$  chemical shift interaction tensors in a peptide bond by three-dimensional solid-state NMR, *J. Am. Chem. Soc.* **117**, 6148–6149.
- Oas, T. G., Hartzell, C. J., Dahlquist, F. W., and Drobny, G. P. (1987) The amide  $^{15}\text{N}$  chemical shift tensors of four peptides determined from  $^{13}\text{C}$  dipole-coupled chemical shift powder patterns, *J. Am. Chem. Soc.* **109**, 5962–5966.
- Hong, M., Gross, J. D., Hu, W., and Griffin, R. G. (1998) Determination of the peptide torsion angle  $\phi$  by  $^{15}\text{N}$  chemical shift

- and  $^{13}\text{Ca}$ - $^1\text{Ha}$  dipolar tensor correlation in solid-state MAS NMR, *J. Magn. Reson.* 135, 169–177.
42. Thayer, A. M., and Kohler, S. J. (1981)  $^{31}\text{P}$  NMR of hexagonal and isotropic phospholipid phases, *Biochemistry* 20, 6831.
  43. Seelig, A., and Seelig, J. (1974) Dynamic structure of fatty acyl chains in phospholipid bilayers by  $^2\text{H}$  NMR, *Biochemistry* 13, 4839.
  44. Huster, D., Yao, X., Jakes, K., and Hong, M. (2002) Conformational changes of colicin Ia channel-forming domain upon membrane binding: a solid-state NMR study, *Biochim. Biophys. Acta* 1561, 159–170.
  45. Cornell, B. A., Separovic, F., Baldassi, A. J., and Smith, R. (1988) Conformation and orientation of gramicidin A in oriented lipid bilayers measured by solid-state carbon- $^{13}\text{C}$  NMR, *Biophys. J.* 53, 67–76.
  46. Picard, F., Paquet, M.-J., Dufourc, E. J., and Auger, M. (1998) Measurement of the lateral diffusion of dipalmitoylphosphatidylcholine adsorbed on silica beads in the absence and presence of melittin: a  $^{31}\text{P}$  two-dimensional exchange solid-state NMR study, *Biophys. J.* 74, 857–868.
  47. Gennis, R. B. (1989) *Biomembranes: Molecular Structure and Function*, Springer, New York.
  48. Mathews, C. K., and Holde, K. E. v. (1996) *Biochemistry*, Benjamin and Cummings, Menlo Park, CA.
  49. Sankaram, M. B., and Thompson, T. E. (1990) Modulation of phospholipid acyl chain order by cholesterol. A solid-state  $^2\text{H}$  nuclear magnetic resonance study, *Biochemistry* 29, 10676–10684.
  50. Wishart, D. S., Bigam, C. G., Holm, A., Hodges, R. S., and Sykes, B. D. (1995)  $^1\text{H}$ ,  $^{13}\text{C}$  and  $^{15}\text{N}$  random coil NMR chemical shifts of the common amino acids. I. Investigations of nearest neighbor effects, *J. Biomol. NMR* 5, 67–81.
  51. Wishart, D. S., Bigam, C. G., Yao, J., Abildgaard, F., Dyson, H. J., Oldfield, E., Markley, J. L., and Sykes, B. D. (1995)  $^1\text{H}$ ,  $^{13}\text{C}$ , and  $^{15}\text{N}$  chemical shift referencing in biomolecular NMR, *J. Biomol. NMR* 6, 135–140.
  52. Marcotte, I., Wegener, K. L., Lam, Y.-H., Chia, B. C. S., Planque, M. R. R. d., Bowie, J. H., Auger, M., and Separovic, F. (2003) Interaction of antimicrobial peptides from Australian amphibians with lipid membranes, *Chem. Phys. Lipids* 122, 107–120.
  53. Mui, B. L. S., Dobreiner, H. G., Madden, T. D., and Cullis, P. R. (1995) Influence of transbilayer area asymmetry on the morphology of large unilamellar vesicles, *Biophys. J.* 69, 930–941.
  54. Lee, S., Furuya, T., Kiyota, T., Takami, N., Murata, K., Niidome, Y., Bredeisen, D. E., Ellerby, H. M., and Sugihara, G. (2001) De novo designed peptide transforms Golgi-specific lipids into Golgi-like nanotubules, *J. Biol. Chem.* 276, 41224–41228.
  55. Farsad, K., and De Camilli, P. (2003) Mechanisms of membrane deformation, *Curr. Opin. Cell Biol.* 15, 372–381.
  56. Yager, P., and Schoen, P. E. (1984) Formation of tubules by a polymerizable surfactant, *Mol. Cryst. Liq. Cryst.* 106, 371–381.
  57. Schnur, J. M., Ratna, B. R., Selinger, J. V., Singh, A., Jyothi, G., and Eastwaran, K. R. K. (1994) Diacetylenic lipid tubules: experimental evidence for a chiral molecular architecture, *Science* 264, 945–947.
  58. Rudolph, A. S., Ratna, B. R., and Kahn, B. (1991) Self-assembling phospholipid filaments, *Nature* 352, 52–55.
  59. Zarif, L. (2002) Elongated supramolecular assemblies in drug delivery, *J. Controlled Release* 81, 7–23.
  60. Jung, H. T., Lee, S. Y., Kaler, E. W., Coldren, B., and Zasadzinski, J. A. (2002) Gaussian curvature and the equilibrium among bilayer cylinders, spheres, and discs, *Proc. Natl. Acad. Sci. U.S.A.* 99, 15318–15322.
  61. Safran, S. A., Pincus, P., and Andelman, D. (1990) Theory of spontaneous vesicle formation in surfactant mixtures, *Science* 248, 354–356.
  62. Sheetz, M. P., and Singer, S. J. (1974) Biological membranes as bilayer couples. A molecular mechanism of drug-erythrocyte interactions, *Proc. Natl. Acad. Sci. U.S.A.* 71, 4457–4461.
  63. Villalain, J. (1996) Location of cholesterol in model membranes by magic-angle-sample-spinning NMR, *Eur. J. Biochem.* 241, 586–593.
  64. Branden, C., and Tooze, J. (1991) *Introduction to protein structure*, Garland Publishing, New York.

BI036243W